Resolution enhancement of pump-probe microscopy with an inverse-annular spatial filter

T. Kobayashi, K. Kawasumi, J. Miyazaki, and K. Nakata

CrossMark
click for updates

Resolution enhancement of pump-probe microscopy with an inverse-annular spatial filter

T. Kobayashi,[1,2,3,4,a] K. Kawasumi,[1] J. Miyazaki,[1,2] and K. Nakata[1,2]
[1]*Advanced Ultrafast Laser Research Center, The University of Electro-Communications, 1-5-1 Chofugaoka, Chofu, Tokyo 182-8585, Japan*
[2]*JST, CREST, K' Gobancho, 7, Gobancho, Chiyoda-ku, Tokyo 102-0076, Japan*
[3]*Department of Electrophysics, National Chiao-Tung University, Hsinchu 300, Taiwan*
[4]*Institute of Laser Engineering, Osaka University, 2-6 Yamada-oka, Suita, Osaka 565-0971, Japan*

We have introduced a pupil filter, an inverse-annular pupil filter in a pump-probe photothermal microscope, which provides resolution enhancement in three dimensions. The resolution is probed to be improved in lateral and axial resolution by imaging experiment using 20 nm gold nanoparticles. The improvement in X (perpendicular to the common pump and probe polarization direction), Y (parallel to the polarization direction), and Z (axial direction) are by 15±6, 8±8, and 21±2 % from the resolution without a pupil filter. The resolution enhancement is even better than the calculation using vector field, which predicts the corresponding enhancement of 11, 8, and 6 %. The discussion is made to explain the unexpected results. We also demonstrate the photothermal imaging of thick biological samples (cells from rabbit intestine and kidney) stained with hematoxylin and eosin dye with the inverse-annular filter. © *2016 Author(s). All article content, except where otherwise noted, is licensed under a Creative Commons Attribution (CC BY) license (http://creativecommons.org/licenses/by/4.0/).* [http://dx.doi.org/10.1063/1.4967948]

I. INTRODUCTION

Pump-probe microscopy can provide images by detecting changes in probe light intensity induced by stimulated emission, photoinduced absorbance change (PA) or photothermal (PT) effect in either transmission or reflection mode. This technique has various applications. They include the identification of pigments in historical artworks, measurements of carrier dynamics in single quantum well, lifetime measurements of fluorescent samples, and non-invasive characterization of melanocytes.[1–4] Especially, in bio-imaging, pump-probe microscopy can be applied in a wide range of biological tissues regardless of whether the sample is fluorescent or not, with sub-diffraction resolution. Xie et al. developed pump-probe microscopy using stimulated emission and imaged distributions of chromoproteins in live Escherichia coli cells.[5] The pump and probe beams were supplied by high intensity, high repetition rate femtosecond lasers, and a lock-in detection scheme[5] was used to reduce probe noise.[6] Photothermal imaging using pump-probe technique was also applied to biological tissues doped with metallic nanoparticles, which induces the deflection of probe beam by refractive index change due to photothermal effect.[7–9]

In our previous works, we demonstrated pump-probe microscopy without using Ti:sapphire laser based femtosecond pulse lasers, optical parametric amplifiers, or high speed detectors.[10–15] Our pump-probe system is equipped with two intensity-modulated laser diodes (LDs), a lock-in amplifier, and an auto-balanced detector to remove the probe noise. It could achieve high sensitivity detection at a low cost. Especially the laser diodes are nearly 50 times less expensive than ultrashort pulse lasers. In addition, another advantage of using laser diodes is the capability of tuning of the LD wavelength and

---

[a]Electronic mail: kobayashi@ils.uec.ac.jp

modulation frequency. We can easily change the laser wavelength by changing the LD element, and can select the modulation frequency (~MHz) by modulating the laser diode (LD) current. Recently, we implemented an annular pupil filter into a microscope before the objective lens to improve the spatial resolution.[12] A doughnut-shaped beam created by this filter is focused through an objective lens and forms a sharp main peak with unwanted side lobes in the focal plane.[16,17] Side lobes are the satellite ring peaks appearing in the diffraction pattern by a circular aperture. Its structure is given by the first-order Bessel function $J_1(r)$ which has a dumped oscillatory feature along the radial direction (r). The spatial resolution of pump-probe microscope can be approximated with the product of intensity profiles of pump and probe beams because the pump-probe signal is based on the bilinear interaction between two beams mediated by the sample.[10] Because of the effective nonlinearity induced by the bi-linearity, the pump-probe microscope has spatial resolution better than conventional optical microscopes. This mechanism of bi-linearity of pump and probe intensity is especially powerful to the biological sample which does not have strong absorption in the visible range being used for probing. In the case of semiconductors reflection mode can be utilized which is expected to detect the change in signal intensity of the Mie scattering in the backward direction. An annular pupil filter performed further improvement of the lateral resolution over diffraction limit.[12] Although relatively strong side lobes appear near the main peak due to diffraction, they can be suppressed because of difference in the locations of the side lobe peaks due to the different wavelength of pump and probe beams.[12] The diffraction fringe intensities are decreased by the cancellation of them.

The annular pupil filter is an effective method to increase the lateral resolution and very easy to introduce into the microscope, however, the axial resolution becomes more than twice lower than that without pupil filter.[12,18] Therefore, it is not suitable for the construction of three-dimensional (3D-) images of thick biological samples. In this paper, to increase not only the lateral but also the axial resolution, we introduced a new pupil filter, an inverse-annular pupil filter. It has been claimed theoretically that an inverse annular filter achieved a significant enhancement of the resolution of the fluorescence microscopy region both in the lateral and axial directions,[19] but this claim has not been proven experimentally. Furthermore, the theoretical enhancement in the paper has been discussed only for the conventional fluorescence microscopy, not for pump-probe microscopy including PT imaging. It is expected that combination of the nonlinearity in the PT imaging and removal of the interference taking place in the structured illumination, further resolution enhancement is expected. Furthermore even clearer image can be expected by the aforementioned side lobe cancellation in both lateral and axial directions.

In this study, further improvement of the image quality can be attained by cancellation of the fringe patterns appearing in the lateral and axial intensity distributions of both pump and probe beams. We also theoretically calculate the expected improvements in resolution. To increase not only the lateral but also the axial resolution, we introduced an inverse-annular pupil filter rather than an annular pupil filter. The resolution is evaluated experimentally using gold nanoparticles (GNP) with a 20-nm diameter. The resolution powers evaluated in the X (perpendicular to the common pump and probe polarization direction), Y (parallel to the polarization direction), and Z (axial) directions are found to be improved by 15±6, 8±8, and 21±2 % relative to those without a pupil filter. The standard deviation is obtained by the properly estimated background signal inevitable in the imaging. The experimental results, which are even better than our theoretical predications, are discussed. We also demonstrate PT imaging of thick biological samples (cells from rabbit intestine and kidney) stained with hematoxylin and eosin dye with enhanced resolution.

II. INVERSE-ANNULAR FILTER

First, we theoretically estimate the spatial resolution of the pump-probe signal using a vector diffraction model with three illumination modes produced using three different sets of a pupil and filters, including inverse-annular illumination. To investigate the differences in spatial resolution among the three modes, we used the following parameters for the three filters, as illustrated in Fig. 1(a): pupil diameter Φ_1, internal diameter of the annular filter Φ_2, and pupil diameter of the objective lens Φ_3. The values selected for these parameters are listed in Table I. The radial coordinate is represented in terms of numerical aperture (NA).
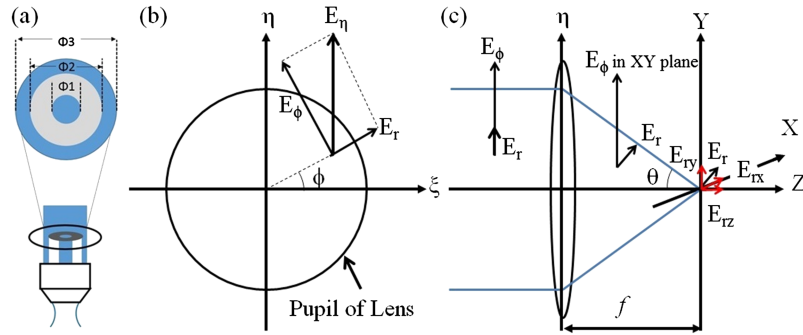
FIG. 1. (a) Structure of inverse-annular filter before the objective pupil. The structures of circular, annular, and inverse annular filters are described with different parameter sets of (Φ_1, Φ_2, Φ_3). This filter can be transmitted through the center and annular parts of the beams (blue-area). Diameters of the central and annular parts are expressed by Φ_1 and Φ_2, respectively. Φ_3 is the pupil diameter, which is determined by the objective lens. (b), (c) Electric field components in a lateral plane (b) and around a focal point (c). In this figure, linear polarized laser is illuminated with polarization direction of η-axis.

TABLE I. Aperture parameter sets of the filters for the three illumination modes.

Illumination mode	Φ_1 [mm]	Φ_2 [mm]	Φ_3 [mm]
Circular	0	0	8.55
Annular	0	5.8	8.55
Inverse annular	3.1	6.3	8.55

Inverse-annular illumination produces both circular and annular beams (blue area in Fig.1 (a)). These beam areas determine the 3D spatial resolution in microscopy based on point-scanning systems.[19,20] While Φ_3 depends on the focal length and NA of the objective lens, Φ_1 and Φ_2 can be set optimized by changing the beam-blocking area (gray area). In this study, we set $\Phi_1 = 3.1$ mm, $\Phi_2 = 6.3$ mm and used the objective lens parameter $\Phi_3 = 8.55$ mm. The vector diffraction theory used can determine the resolution with high accuracy in comparison with the scalar diffraction theory because the former includes polarization dependence in each direction. Both pump and probe fields in our microscope are linearly polarized parallel to Y-direction, so the intensity distribution on the focal plane is different between the parallel and perpendicular directions to the polarization.[21,22]

Fig. 1 (b) shows the electric field components in a lateral plane (XY). The illuminating laser is linearly polarized along the η-axis (or Y-axis), and the electric fields in the radial and declination directions in the microscopic region can be written as:

$$E_r = E_\eta sin\varphi \tag{1}$$

$$E_\varphi = E_\eta cos\varphi, \tag{2}$$

where E_η is the electric field component of the laser along the η-axis. E_r and E_φ can be resolved into X, Y, and Z components, as illustrated in Fig. 1(c) and given as:

$$E_{rx} = E_r cos\theta cos\varphi \tag{3}$$

$$E_{ry} = E_r cos\theta sin\varphi \tag{4}$$

$$E_{rz} = E_r sin\theta \tag{5}$$

and

$$E_{\varphi x} = -E_\varphi sin\varphi \tag{6}$$

$$E_{\varphi y} = E_{\varphi} cos\varphi. \tag{7}$$

The components of the electric field amplitude in the X, Y, and Z directions P_x, P_y, and P_z in the microscopic region are obtained as follows after substituting Eqs. (1) and (2) into Eqs. (3)–(7) and

$$P_x = E_{rx} + E_{\varphi x} = E_{\eta} (cos\theta sin\varphi cos\varphi - sin\varphi cos\varphi) \tag{8}$$

$$P_y = E_{ry} + E_{\varphi y} = E_{\eta} \left(cos\theta sin^2\varphi - cos^2\varphi \right) \tag{9}$$

$$P_z = E_{rz} = E_{\eta} sin\theta sin\varphi. \tag{10}$$

When an incident plane wave is converted into a convergent spherical wave, correction corresponding to the amplitude variation of the electric field $(cos\theta)^{0.5}$ is required.[23] Electric field amplitudes of the X, Y, and Z-axis directions E_x (x, y, z), E_y (x, y, z), and E_z (x, y, z) including the correction term are determined by the Fourier transformation of Eqs. (8), (9), and (10) in a proper integration range. The electric field amplitude distribution are then described as follows

$$E_x (x, \ y, \ z) = C \int \int P_x(\theta, \phi)\sqrt{cos\theta}exp\left\{-ik\left(\xi x + \eta y + \zeta z\right)\right\} dS \tag{11}$$

$$E_y (x, \ y, \ z) = C \int \int P_y(\theta, \phi)\sqrt{cos\theta}exp\left\{-ik\left(\xi x + \eta y + \zeta z\right)\right\} dS \tag{12}$$

$$E_z (x, \ y, \ z) = C \int \int P_z(\theta, \phi)\sqrt{cos\theta}exp\left\{-ik\left(\xi x + \eta y + \zeta z\right)\right\} dS \tag{13}$$

Here, k is the wave number and is equal to $2\pi n/\lambda$, θ is the polar coordinate, and dS is the microscopic region on the convergence spherical plane given by $dS = \frac{d\xi d\eta}{cos\theta} = sin\theta d\theta d\phi$. The Cartesian coordinates representing the pupil plane, ξ and η, are given by

$$\xi = \sqrt{\xi^2 + \eta^2} \cos\phi = sin\theta cos\phi \tag{14}$$

$$\xi = \sqrt{\xi^2 + \eta^2} \cos\phi = sin\theta cos\phi \tag{15}$$

Substituting Eqs. (14) and (15) into Eqs. (11)–(13), the field amplitudes are obtained as follows

$$E_x (x, \ y, \ z) = C \int \int P_x\sqrt{cos\theta}exp\left\{-ik\left(xsin\theta cos\varphi + ysin\theta sin\varphi + zcos\theta\right)\right\} sin\theta d\theta d\varphi \tag{16}$$

$$E_y (x, \ y, \ z) = C \int \int P_y\sqrt{cos\theta}exp\left\{-ik\left(xsin\theta cos\varphi + ysin\theta sin\varphi + zcos\theta\right)\right\} sin\theta d\theta d\varphi \tag{17}$$

$$E_z (x, \ y, \ z) = C \int \int P_z\sqrt{cos\theta}exp\left\{-ik\left(xsin\theta cos\varphi + ysin\theta sin\varphi + zcos\theta\right)\right\} sin\theta d\theta d\varphi. \tag{18}$$

Converting the integration variable θ to $r = nsin\theta$ in the unit of numerical aperture (NA), Eqs. (16), (17) and (18) can be rewritten as follows:

$$E_x (x, \ y, \ z) = C \int \int A_x exp\left\{-ik\left(rxcos\varphi + rysin\varphi + z\left(1 - (r/n)^2\right)^{\frac{1}{2}}\right)\right\} drd\varphi \tag{19}$$

$$E_y (x, \ y, \ z) = C \int \int A_y exp\left\{-ik\left(rxcos\varphi + rysin\varphi + z\left(1 - (r/n)^2\right)^{\frac{1}{2}}\right)\right\} drd\varphi \tag{20}$$

$$E_z (x, \ y, \ z) = C \int \int A_z exp\left\{-ik\left(rxcos\varphi + rysin\varphi + z\left(1 - (r/n)^2\right)^{\frac{1}{2}}\right)\right\} drd\varphi \tag{21}$$

with

$$A_x = \frac{r}{n}\left[\left\{1 - \left(\frac{r}{n}\right)^2\right\}^{\frac{1}{4}} - \left\{1/\left(1 - \left(\frac{r}{n}\right)^2\right)\right\}^{\frac{1}{4}}\right] sin\varphi cos\varphi$$

$$A_y = \frac{r}{n}\left[\left\{1/\left(1 - \left(\frac{r}{n}\right)^2\right)\right\}^{\frac{1}{4}} sin^2\varphi + \left\{1 - \left(\frac{r}{n}\right)^2\right\}^{\frac{1}{4}} cos^2\varphi\right]$$

$$A_z = \frac{r^3}{n} \left\{ 1 / \left(1 - \left(\frac{r}{n} \right)^2 \right)^{\frac{1}{4}} \right\} sin\varphi.$$

The light intensity distribution in the image volume, $I = |E_x(x, y, z)|^2 + |E_y(x, y, z)|^2 + |E_z(x, y, z)|^2$, is calculated by integration over the open aperture area represented by pitch coordinates of the NA, r, and declination angle φ. The integration ranges in the radial direction are set as $0 < r < 0.95$ for no filter (circular illumination), $0.68 < r < 0.95$ for the annular filter and $0 < r < 0.34$ and $0.70 < r < 0.95$ for the inverse annular filter in the unit of numerical aperture NA. The integration range in the declination angle is $0 < \varphi < 2\pi$ for all calculation.

   Calculated results of the resolution improvement in the pump-probe microscopy with circular illumination are shown in Fig. 2. Since signal intensity distribution of the pump-probe signal, $I_{sig}(x, y, z)$ is given by $I_{sig}(x, y, z) = I_{pu}(x, y, z) \times I_{pr}(x, y, z)$.[9] The peripheral ring structures introduced by diffraction in both the pump and probe beams can be cancelled out because the ring radii of the pump and probe are different, as the two beams are of different wavelength. This can be confirmed in Fig. 2, which shows resolution improvement of the pump-probe measurement by the similar calculation by the PSF. The improvements of the resolution in XY and XZ planes are 37 - 39 %, respectively, as shown in Table II based on Fig. 2. Thus, in the case of PT imaging, inverse-annular illumination is even more advantageous.

   The calculated results of intensity distribution are depicted in Fig. 3, which shows distributions in the XY (a1, b1, c1) and XZ (a2, b2, c2) planes of the pump-probe signal by circular illumination (a, without the filter, $\Phi_1 = \Phi_2 = 0$ mm), annular illumination (b, $\Phi_1 = 0$ mm, $\Phi_2 = 5.8$ mm), and inverse-annular illumination (c). The polarization direction is along Y-axis. Fig. 4 shows cross-section profiles and Table III lists the calculated resolution of lateral (X- and Y-) directions and axial (Z-) direction in the case of Y-polarization probe field in terms of the full width a half maximum (FWHM) values of the PSF. As shown in these figures and the table, the improvements of resolution with annular filter from the circular case in the lateral direction are 15 and 19 %, respectively, in parallel (X-axis) and perpendicular (Y-axis) directions to the laser field (X-axis). However, the enhancement is with the expense of the lowering of the resolution in the axial direction by nearly 50% reduction indicating that the distribution is increased to 1.5 times in the spatial spread width of the image of delta-function like object. In contrast to the annular filter case, the improvements gained using the inverse-annular
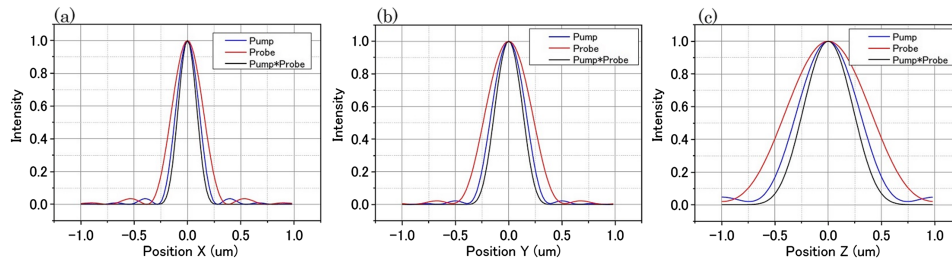

FIG. 2. Calculated results of the intensity distribution to show the resolution improvement in pump-probe microscopy in X-axis (a), Y-axis (b) and Z-axis (c). The resolution of the intensity for the pump-probe microscopy (black lines) is better than the resolution for the pump (blue lines) and the probe (red line) laser. In the calculation, the wavelengths of the pump and probe laser are 488 nm and 660 nm, respectively.

TABLE II. FWHMs of lateral intensity distributions by the pump beam, the probe beam, and the pump-probe signal in Fig.2; Improvement of PP results with two colors from the cases of single color experiment.[a]

Image direction	Pump (Blue) [nm]	Probe (Red) [nm]	Pump-Probe (PP) (Black) [nm]	Improvement PP /Pump	Improvement PP /Probe
X	234	315	197	16 %	37 %
Y	337	456	285	15 %	37 %
Z	635	863	527	17 %	39 %

[a]The laser wavelengths of pump and probe are 488 nm and 660 nm, respectively. The refractive index used in the calculation is set to be 1 (air).
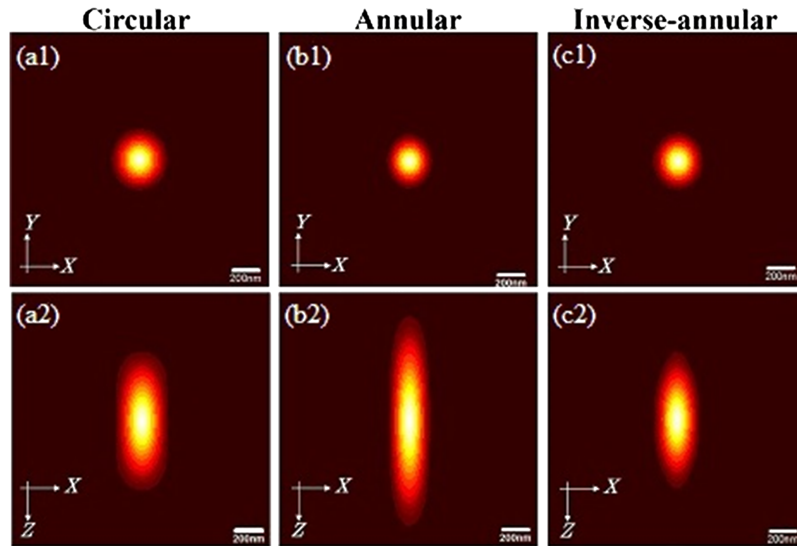
FIG. 3.   Intensity profile of images of a single GNP with 20nm-diameter near the focal point of the objective lens in the XY (a1, b1, and c1) and XZ (a2, b2, and c2) planes calculated for pump-probe experiment with different apertures. The wavelengths of pump and probe beams are 488 nm and 660 nm, respectively. Numerical aperture (NA) of the objective lens is 0.95.
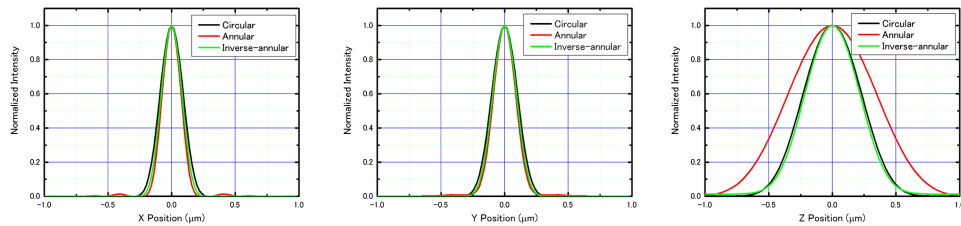

FIG. 4.   Cross-section profiles of the intensities of the pump-probe images shown in Fig. 3 in X, Y, and Z directions. The width of the PSF in the X- and Y-axis direction is smaller, but the width in the Z-axis direction is much larger in annular illumination case (red lines) than the circular illumination case (black lines). The resolution is also improved in the inverse-annular illumination (green lines) in any direction.

TABLE III.   FWHMs of the intensity distribution of images for infinitely small particles by the pump-probe calculation in Fig. 3.[a]

Imaging direction	Circular [nm]	Annular [nm]	Inverse-annular [nm]	Improvement (Annular filter)	Improvement (IA filter)
X-axis	208.0	167	186.1	19 %	11 %
Y-axis	232.9	198	214.9	15 %	8 %
Z-axis	527.4	793	494.4	-50 %	6 %

[a]The Laser wavelengths of pump and probe are 488 nm and 660 nm, respectively. The refractive index used in the calculation is set to be 1.5 (PVA film employed as a matrix material in the experiment of resolution evaluation using the gold nanoparticles).

filter compared with the circular aperture case in the directions parallel and perpendicular to the laser field are 8% and 11%, respectively, and 6% improvement can be obtained even in the axial direction.

III. EXPERIMENTAL SETUP

Fig. 5 shows a schematic illustration of our pump-probe microscopy system, which employs two laser diodes (LDs) as the pump and probe light sources. A 488-nm LD (Nichia, NDS4216) and
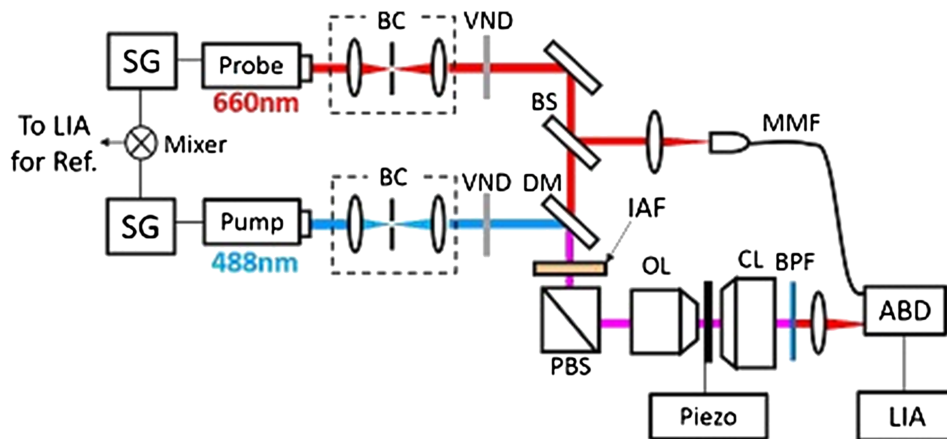
FIG. 5. A scheme of pump-probe microscope system. SG: signal generator, Pump: 488 nm laser diode for pump light, Probe: 660 nm laser diode for probe light, BC: beam collimator, VND: variable neutral density filter, BS: probe beam splitter, DM: dichroic mirror, IAF: inverse-annular filter, PBS: polarized beam splitter, OL: objective lens, CL: condenser lens, BPF: band pass filter, ABD: auto-balanced detector, LIA: lock-in amplifier, MMF: multi-mode fiber.

a 660-nm LD (Mitsubishi, ML101U29) are used for the pump and probe beams, respectively. The two beams are modulated at frequencies of ω_1 (pump) and ω_2 (probe) using signal generators (SGs) and are introduced to beam collimators that contain spatial filters. After the beams are combined using a dichroic mirror, they irradiate the sample after passing through an objective lens (Olympus, UPLSAPO 40X2) with a NA of 0.95. Diameters of the pump and probe laser calculated by using $1.22 \times \lambda$/NA are 626.7 nm and 847.6 nm, respectively. A condenser lens collects the transmitted probe beam from the sample and introduces the light to a detector. To remove the probe noise, we use an auto-balanced detector (Newfocus, Nirvana) containing two photodiodes; one is for the probe beam and the other is for a reference beam split off from the probe beam by a beam splitter (BS in Fig. 5) placed before a dichroic mirror (DM in Fig. 5).[10–15] The intensity noise of these beams is canceled using this balance detection scheme. Thus, shot-noise limited sensitivity can be achieved when the probe beam power is higher than ~10 mW on the photodiode surface.[10] A lock-in amplifier (Signal Recovery, 7270) detects the signal at the beat frequency $|\omega_1 - \omega_2|$. In this study, we set modulation frequencies ω_1 and ω_2 to 1.000 MHz and 1.015 MHz, respectively. A frequency mixer (Mini-circuit, ZAD-1) generates $|\omega_1 - \omega_2|$ component for a reference signal of the lock-in amplifier. Closed loop piezo-actuators (Thorlabs, MAX311D) scan the sample in the three axial directions. The time constant of the lock-in amplifier is 0.5 ms, and the dwell time is 1.0 ms in the gold nanoparticle experiments. The pixel number in the image of the GNP is 300×300 and hence the frame time of the image is 90 seconds and the motor driven stage step is 50 nm. The time constant of the lock-in amplifier and the dwell time are 0.5 ms and 1 ms, respectively, in the biological sample imaging. The pixel number is 800×800 and hence the frame time of the image is 640 seconds and the stage step is 18.75 nm.

To improve the 3D spatial resolution, an inverse-annular filter (IAF) is installed before the polarization beam splitter (PBS). The beam blocking area of this filter is made by affixing a metal washer (clip plate, facing ring) onto an optical window. A holder mounting the IAF is adjusted to produce a symmetric inverse-annular beam in the objective pupil plane.

IV. RESULTS

A. Evaluation of 3D spatial resolution by imaging gold nanoparticle (GNP)

To evaluate the improvement in the 3D spatial resolution, we capture PT images of 20-nm gold nanoparticles (GNPs) dispersed in a polyvinyl alcohol (PVA) film. Although the GNPs have a large absorption cross section due to their plasmon resonance, the luminescence yield is extremely small.[9] Thus, the pump beam causes an increase in temperature around the GNPs due to the PT effect, which

in turn results in decrease in the local refractive index of the PVA at the modulation frequency ω_1. This index variation forming a thermal concave lens leads to a deflection of the probe beam and a time-dependent change in the probe beam intensity that is detected by the ABD. The beat signal at $|\omega_1 - \omega_2|$ is also generated by the bilinear interaction of the pump and probe fields in the sample,[12] which is detected using the lock-in scheme.

The sample is scanned in the focal plane (XY-plane, Figs. 6 (a) and 6(c)) and optical axis plane (XZ-plane, Figs. 6(b) and 6(d)) with and without the IAF (i.e., inverse-annular and circular illumination), respectively. The pump and probe powers are respectively set to 3.8 mW and 0.3 mW for inverse-annular illumination case and to 1.6 mW and 0.22 mW for circular illumination case. The signal to noise ratios of the data of inverse-annular (black points) and circular (red points) illumination in Fig. 6 are 7.2 ± 2.8 and 11.5 ± 1.5 (e), 8.2 ± 3.5 and 12.8 ± 3.4 (f), 11.0 ± 6.3 and 6.5 ± 2.4 (g), respectively. The signal to background ratios of the data of inverse-annular (black dots) and circular (red dots) illumination mode in Fig. 6 are 12.1 ± 1.4 and 12.4 ± 1.1((e) along X), 10.8 ± 0.8 and 11.2 ± 0.9 ((f) along Y), 19.5 ± 1.8 and 11.9 ± 0.7 ((g) along Z), respectively. The reproducibility was checked by doing experiment for 5 to 10 GNPs depending on the illumination case. In each case the spatial dependence of the PT signal intensities is fitted with a Gaussian function using the least squares method. The data values in Fig. 6 are summarized in Table IV. The values for experimental results ("Observed Circular" and "Observed Inverse annular" columns) in the Table IV are mean values of statistical analysis of the FWHM values obtained by the Gaussian fit of the intensity distribution of several GNP images and the values after ± are the standard deviation of the statistical analysis. The spatial dependent intensities are averaged over the measured GNPs and the standard deviations of the FWHMs are calculated. The signal intensity of inverse annular illumination case is substantially weaker than the circular illumination case; therefore larger number of GNPs was measured for the inverse annular illumination case. Table IV clearly shows that the
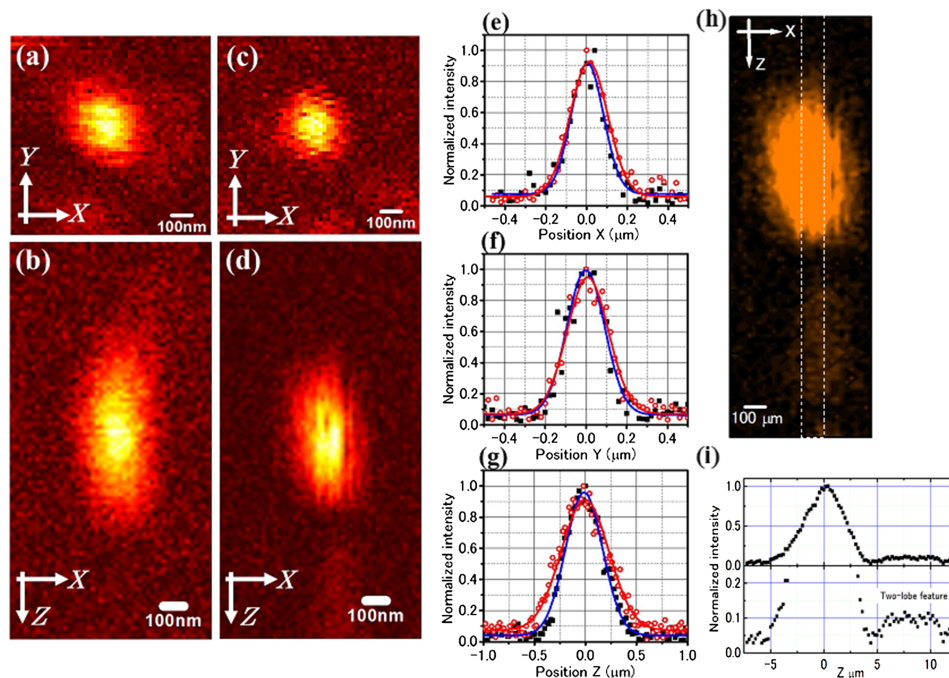

FIG. 6. Photothermal images of a single GNP in PVA film and their intensity profiles. Circular illumination configuration in XY (a) and XZ-plane (b). Inverse-annular illumination configuration in XY (c) and XZ-plane (d). XZ-plane images are obtained directly by XZ scanning with piezo stage. Intensity cross-section profiles of circular (red open dots) and inverse-annular illumination (black filled squares) in X, Y, and Z-axis directions are shown in (e), (f), and (g), respectively. Red and blue solid lines are Gaussian fitting curves in circular and inverse-annular illumination, respectively. Image with the two-lobe feature is shown in (h) and intensity along the axial direction integrated between two lines in (h) is shown in (i). The lower part shows the enlarged profile in the upper part.

TABLE IV. FWHMs of the photothermal intensity by the pump-probe calculation and the standard deviations of the Gaussian fitting to the observed intensity distributions of GNP images in Fig. 6.

Imaging direction	Calculated Circular [nm]	Observed Circular [nm]	Calculated Inversed-annular [nm]	Observed Inverse-annular [nm]	Improvement by calculation	Improvement by experiment
X-axis	208.0	219±6	186.1	187±8	11 %	15±6 %
Y-axis	232.9	239±10	214.9	219±11	8 %	8±8 %
Z-axis	527.4	550±10	494.4	430±8	6 %	21±2 %

FWHM of the "inverse annular illumination" case is always smaller than the FWHM of the "circular" cases even the standard deviation is taken into account. In the X and Y-axis directions, FWHMs for the inverse-annular illumination are smaller than in the circular illumination. In addition, each FWHM value agrees well with its corresponding value calculated using vector diffraction theory, in Table III. The resolution enhancements in the X and Y-axis directions are evaluated to be 15 ± 6 %, 8 ± 8 %, and 21 ± 2 %, respectively. Difference in resolution enhancement between the X and Y-axis directions is due to the linear polarizations of the pump and probe beams are both along Y-axis. In the Z-axis direction, the resolution obtained using inverse-annular illumination is also better than the conventional circular illumination. Surprisingly, the enhancements in resolution obtained experimentally are even better than those predicted theoretically, which is discussed in the following.

Selmke and coworkers[24] discussed the dependence of the image resolution on the relative position of the pump and probe focal points. They found that the apparent lateral resolution depends sensitively on the relative focal positions of the two beams. In some cases, the image along the axial direction had two lobes with a π-phase jump, resulting in an apparent reduction in the axial direction caused by a cancellation between the two lobes opposite signs due to the π-phase jump. Even though this effect may slightly distort the image, the location of the image of signal-generating particle does not change much and therefore can be used in actual imaging when a precise axial intensity distribution of the target image is not required. By removing one of the lobe by shifting the relative position of the pump or probe focal plane, the two-lobe feature is detected as shown in Figs. 6 (h) and (i). This is because of the relative contributions of positive lobe (phase 0) and negative lobe (phase π) are changed by the probe position with respect to the pump peak position. Because of this effect, we observe minor changes smaller than 10% in the size of the image structure when we move the focal position in the axial direction as expected and observed previously in reference[24] and in our experiment.[11,12]

B. Biological imaging

We also performed PT imaging of biological systems using a rabbit small intestine and kidney as samples. The resolution was evaluated for tissues stained with hematoxylin and eosin (HE). The thickness of the small intestine sample is about 10 μm. HE staining has been routinely used in path morphology and histopathology, e.g., in the diagnosis of tumor progression.[25] Since HE can be used to stain anionic and cationic structures (e.g., nuclei containing DNA and basic protein),[26] these structures can be distinguished using a bright-field microscope. While eosin has a fluorescence peak around 540 nm in water,[27] hematoxylin is an essentially non-fluorescent pigment,[25,26] and the energy from the excitation laser is instead converted into heat, resulting in the photothermal effect. However we utilize both H and E as the source materials of the PT signal. Even in the case of eosin, it is much more advantageous to utilize the PT effect for imaging because of much higher robustness than fluorescence. Our pump-probe microscope can be used to capture PT images in both regions of a sample stained with eosin and hematoxylin at the same time.

Figs. 7 (a) and 7(b) show the photothermal images of a small intestine taken for a rabbit intestine captured using the circular (a) and the inverse-annular (b) illumination in the focal (XY) plane. The pump and probe powers are 150 μW and 420 μW for (a), and 140 μW and 120 μW for (b), respectively. The signals originating from the elliptical structures in (a) and (b) are particularly well detected. It can be concluded that these regions are cell nuclei, which are primarily stained with hematoxylin
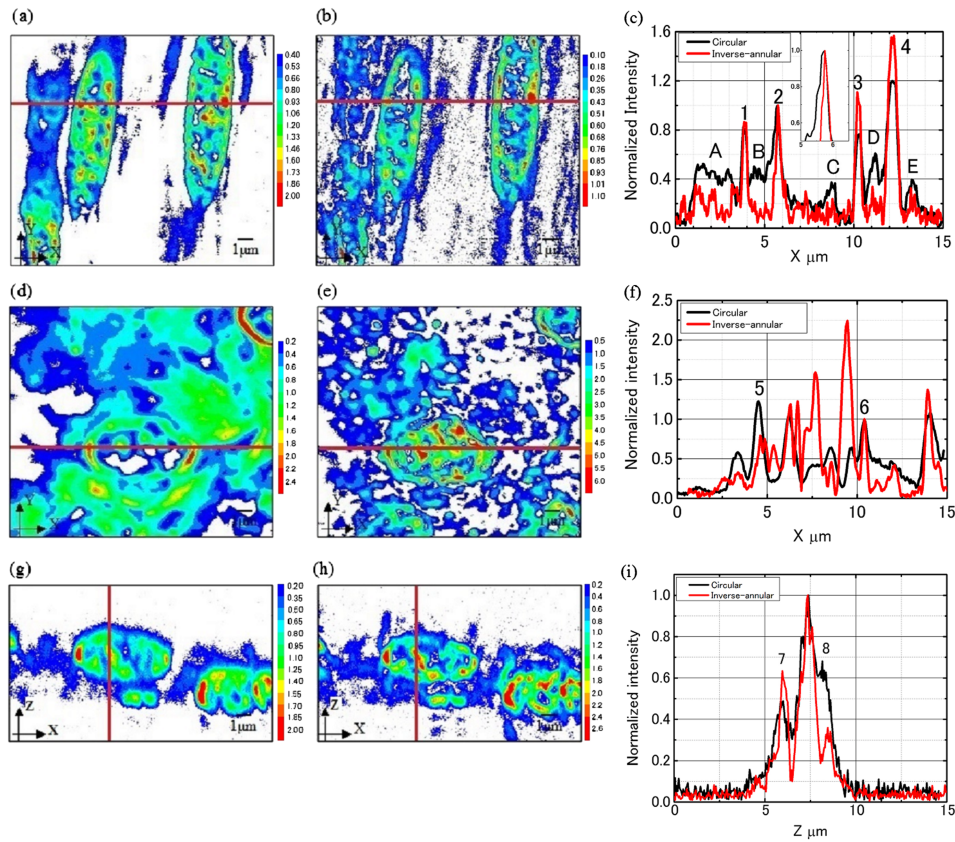
FIG. 7. Images of several biological samples obtained without inverse annular filter (namely with circular illumination) and with inverse annular filter, and comparison in the lateral and axial resolution between the two illuminations. (a) and (b) Photothermal images of cells from rabbit small intestine for the circular and inverse-annular illumination in the focal (XY) plane. The pump and probe power are 140 μW and 120 μW for (a), 150 μW and 420 μW for (b), respectively. (c) The intensity profiles along the black lines in (a) and (b). The red and black solid lines are intensity profiles with the inverse-annular and circular illumination, respectively. Inset shows enlarged view of the peak No. 2. (d) and (e) Photothermal images of cells form rabbit kidney for the circular and inverse-annular illumination in the focal (XY) plane. The pump and probe power are 150 μW and 200 μW for (d), 700 μW and 650 μW for (e), respectively. (f) The intensity profiles along the black lines in (d) and (e). (g) and (h) Photothermal images of cells form rabbit kidney for the circular and inverse-annular illumination in optical axial (XZ) plane. The pump and probe power are 100 μW and 200 μW for (h), 780 μW and 260 μW for (h), respectively. (i) The intensity profiles along the black lines in (g) and (h). All scale bars are 1 μm. Most intense peak in (i) is not used for the resolution discussion because it suffers from the heavily neighboring peaks.

based on their shapes and sizes. To evaluate the lateral resolution of the two images obtained using the two illumination modes, we compare the intensity profiles [Fig. 7(c)] along the black lines in Figs. 7(a) and 7(b). The intensity peaks 1–4 in Fig. 7(c) are clearly separated for both illumination types. Peaks A–E for circular illumination in Fig. 7(c) are missing for inverse-annular illumination, which can be explained as follows. They are considered to originate from signal produced in the domain located with longer distance than the z-direction-lobe size in the inverse-annular mode from the focal plane and thus do not appear when inverse-annular illumination is employed. This is proved by the fact that the absence of missing peaks remains absent when the locations of the focal planes of pump and probe are moved together with the same amount. In the experiment, moving the location of the focal plane is performed by moving the sample in the axial direction. In the GNP experiment, the FWHMs of the signal peak are 550 nm in the circular illumination, and 430 nm in the inverse-annular illumination in Table IV. Therefore, material structures located apart from the focal plane in the axial direction by 200 nm or more can show up by the circular illumination but not by inverse-annular illumination. This result indicates that the resolution is improved not only in the lateral directions but also in the axial direction. In the case of inverse-annular illumination, the signals produced in the

vicinity of focal plane are more efficiently detected, resulting in the observed improvement in the axial resolution over the case of circular illumination.

Figs. 7 (d) and 7(e) show the photothermal images of a rabbit kidney captured using the circular and the inverse-annular illumination in the focal, respectively, in the lateral (XY) plane. The pump and probe power are 150 μW and 200 μW for (d), 700 μW and 650 μW for (e), respectively. The laser is set to the power level, which gives the best photothermal signal with high S/N and no detectable damage. Higher power could give higher signal intensity but suffer from damage during scanning the sample resulting in poor quality of the frame image. The transmittance of the inverse annular filter is 68%. As with the small intestine sample, the intensity profiles [Fig. 7(f)] along the black lines also indicate improvement in the lateral resolution. Figs. 7(g) and 7(h) show the PT images of a sample of rabbit kidney captured using circular and inverse-annular illumination, respectively, in the optical axis (XZ) plane. We have defined the Z-axis as the optical axis in Figs. 7(g) and 7(h). The pump and probe power are 100 μW and 200 μW for (g), 780 μW and 260 μW for (h), respectively. The inner structures of the cell nuclei can be observed clearly with inverse-annular illumination compared to without it. The intensity profiles [Fig. 7(i)] along the black lines in Figs. 7 (g) and 7(h) also indicate an improvement in the axial resolution. From the data in Fig. 7 (c, f, XY plane) and (i, XZ plane), Table V and Table VI, respectively show the FWHM values and the error values in the fitting process of the Gaussian curves to the observed intensity distributions. All the FWHM values of the Gaussian curves are smaller for inverse-annular illumination than for circular illumination by 14–34%. The biological sample has thickness of about 10 μm, hence there is a possibility of existing of neighboring structures on the planes above or below the focal plane causing the modification of the observing image of the target. This may be the reason of the variation of the enhancement depending on the position of target structure. Thus it is hard to remove completely the image deformation. In order to more strictly evaluate the resolution improvement, we analyzed the errors in the evaluation of resolution in terms of the values of FWHM of the intensity distribution of the image shown in Tables V and VI To properly evaluate the effects with and without of the inverse-annular filter, we take the root of the sum of squared error values (corresponding to the widths of the two cases = $(\varepsilon_c^2 + \varepsilon_I^2)^{0.5}$). For peak 1, the root $(542 + 322)$ is approximately 63, which is smaller than the difference of 73 between the cases of with and without shown in Table V. In all other cases, the same inequality condition is satisfied as shown in Tables V and VI. Most intense peak in Fig. 7 (i) is not used for the resolution discussion because it suffers from overlap with the neighboring peaks and the stage step is 18.75 nm. The averages of the fractional increment of resolution by photo-thermal imaging by using inverse annular illumination are 25 ± 8 % in the XY planes and 28 ± 5 % in the XZ plane, respectively.

TABLE V. FWHMs of the PT intensity peaks in XY-plane in Fig. 7.[a]

Peak number	Circular [nm]	Inverse-annular [nm]	Difference of width	$(\varepsilon_c^2 + \varepsilon_I^2)^{0.5}$	Improvement
1	344±54	271±32	73	62.8	21 %
2	478±63	320±35	158	72.1	33 %
3	399±19	263±17	136	25.5	34 %
4	735±61	585±27	150	66.7	20 %
5	458±4	341±67	117	67.1	26 %
6	314±15	271±8	43	17.0	14 %
Average					25(±8) %

[a]ε_c and ε_I: Error values of the peak intensity profiles using circular and inverse annular illumination, respectively.

TABLE VI. FWHMs of the photothermal intensity peaks in XZ-plane in Fig. 7.[a]

Peak number	Circular [nm]	Inverse-annular [nm]	Difference of width	$(\varepsilon_c^2 + \varepsilon_I^2)^{0.5}$	Improvement
7	828±57	552±24	276	61.8	33 %
8	1004±39	774±40	230	55.9	23 %
Average					28 (±5)%

[a]ε_c and ε_I: Error values of the peak intensity profiles using circular and inverse annular illumination, respectively.

V. CONCLUSION

In conclusion, by simply adding an inverse-annular pupil filter to a conventional microscope configuration, the resolution of a pump-probe photothermal microscope has been significantly improved compared to that of a conventional microscope. The resolution in the X (perpendicular to the common pump and probe polarization direction), Y (parallel to the common pump and probe polarization direction), and Z (axial direction) directions has been enhanced by 15±6, 8±8, and 21±2 % relative to the case without the filter. The method has been applied to the photothermal imaging of thick biological samples (rabbit small intestine and kidney cells) stained with hematoxylin and eosin dye.

[1] P. Samineni, A. deCruz, T. E. Villafana, W. S. Warren, and M. C. Fischer, "Pump-probe imaging of historical pigments used in paintings," Opt. Lett. **37**, 1310–1303 (2012).

[2] B. A. Nechay, U. Siegner, M. Achermann, H. Bielefeldt, and U. Keller, "Femtosecond pump-probe near-field optical microscopy," Rev. Sci. Instrum. **70**, 2758–2764 (1999).

[3] C. Y. Dong, C. Buehler, P. T. So, T. French, and E. Gratton, "Implementation of intensity-modulated laser diodes in time-resolved diodes in time-resolved, pump-probe fluorescence microscopy," Appl. Opt. **40**, 1109–1115 (2001).

[4] T. E. Matthews, J. W. Wilson, S. Degan, M. J. Simpson, J. Y. Jin, J. Y. Zhang, and W. S. Warren, "In vivo and ex vivo epi-mode pump-probe imaging of melanin and microvasculature," J. Biomed. Opt. **2**, 1576–1583 (2011).

[5] W. Min, S. Lu, S. Chong, R. Roy, G. R. Holtom, and X. S. Xie, "Imaging chromophores with undetectable fluorescence by stimulated emission microscopy," Nature **461**, 1105–1109 (2009).

[6] L. Wei and W. Min, "Pump-probe optical microscopy for imaging nonfluorescent chromophores," Anal. Bioanal. Chem. **403**, 2197–2202 (2012).

[7] L. Cognet, C. Tardin, D. Boyer, D. Choquet, P. Tamarat, and B. Lounis, "Single metallic nanoparticle imaging for protein detection in cells," P. Natl. Acad. Sci. U.S.A. **100**, 11350–11355 (2003).

[8] P. Vermeulen, L. Cognet, and B. Lounis, "Photothermal microscopy: Optical detection of small absorbers in scattering environments," J. Microsc. **254**, 115–121 (2014).

[9] S. Berciaud, D. Lasne, G. A. Blab, L. Cognet, and B. Lounis, "Photothermal heterodyne imaging of individual metallic nanoparticles: Theory versus experiment," Phys. Rev. B **73**, 045424 (2006).

[10] J. Miyazaki, H. Tsurui, A. Hayashi-Takagi, H. Kasai, and T. Kobayashi, "Sub-diffraction resolution pump probe microscopy with shot-noise limited sensitivity using laser diodes," Opt. Express **22**, 9024–9032 (2014).

[11] J. Miyazaki, H. Tsurui, K. Kawasumi, and T. Kobayashi, "Optimal detection angle in sub-diffraction resolution photothermal microscopy: Application for high sensitivity imaging of biological tissues," Opt. Express **22**, 18833–18842 (2014).

[12] J. Miyazaki, K. Kawasumi, and T. Kobayashi, "Resolution improvement in laser diodes-based pump probe microscopy with an annular pupil filter," Opt. Lett. **39**, 4219–4222 (2014).

[13] J. Miyazaki, H. Tsurui, K. Kawasumi, and T. Kobayashi, "Simultaneous dual-wavelength imaging of nonfluorescent tissues with 3D subdiffraction photothermal microscopy," Opt. Exp. **23**(3), 3647–3656 (2015).

[14] J. Miyazaki, H. Tsurui, K. Kawasumi, and T. Kobayashi, "Sensitivity enhancement of photothermal microscopy with radially segmented balanced detection," Opt Lett. **40**(4), 479–482 (2015).

[15] J. Miyazaki, H. Tsurui, and T. Kobayashi, "Reduction of distortion in photothermal microscopy and its application to the high resolution three-dimensional imaging of nonfluorescent tissues," Biomed. Opt. Exp. **6**(9), 3217–3224 (2015).

[16] B. Sick and B. Hech, "Orientational imaging of single molecules by annular illumination," Phys. Rev. Lett. **85**, 4482–4485 (2000).

[17] J. Kim, D. C. Kim, and S. H. Back, "Demonstration of high lateral resolution in laser confocal microscopy using annular and radially polarized light," Microsc. Res. Techniq. **72**, 441–446 (2009).

[18] K. Kitamura, K. Sakai, and S. Noda, "Sub-wavelength focal spot with long depth of focus generated by radially polarized, narrow-width annular beam," Opt. Express **18**, 4518–4525 (2010).

[19] M. M. Corral, P. Andres, C. J. Z. Rodriguez, and M. Kowalczyk, "Three-dimensional superresolution by annular binary filters," Opt. Commun. **165**, 267–278 (1999).

[20] M. M. Corral, P. Andres, J. O. Castaiieda, and G. Saavedra, "Tunable axial superresolution by annular binary filters. Application to confocal microscopy," Opt. Commun. **119**, 491–498 (1995).

[21] B. Richards and E. Wolf, "Electromagnetic diffraction in optical systems. II. Structure of the image field in an aplanatic system," Proc. Roy. Soc. London A **253**, 358–379 (1959).

[22] K. S. Youngworth and T. G. Brown, "Focusing of high numerical aperture cylindrical-vector beams," Opt. Express **7**, 77–87 (2000).

[23] M. Shibuya, and H. Ooki, 回折と結像の光学 (Asakura Publishing Co. Ltd, 2005), ISBN: 978-4-254-13731-6 C3342.

[24] M. Selmke, M. Braun, and F. Cichos, "Photothermal single-particle microscopy: Detection of a nanolens," Nano Lett. **6**, 2741–2749 (2012).

[25] M. W. Conklin, P. P. Provenzano, K. W. Eliceiri, R. Sullivan, and P. J. Keely, "Fluorescence lifetime imaging of endogenous fluorophores in histopathology sections reveals differences between normal and tumor epithelium in carcinoma in situ of the breast," Cell Biochem. Biophys. **53**, 145–157 (2009).

[26] J. M. Apgar, A. Juarranz, J. Espada, A. Villanueva, M. Canete, and J. C. Stockert, "Fluorescence microscopy of rat embryo sections stained with haematoxylin–eosin and Masson's trichrome method," J. Microsc. **191**, 20–27 (1997).

[27] H. F. de Carvalho and S. R. Taboga, "Fluorescence and confocal laser scanning microscopy imaging of elastic fibers in hematoxylin-eosin stained sections," Histochem. Cell Biol. **106**, 587–592 (1996).